Time-of-flight mass measurements of neutron-rich chromium isotopes up to N=40 and implications for the accreted neutron star crust

Z. Meisel *et al.*

Phys. Rev. C **93**, 035805 — Published 22 March 2016

DOI: 10.1103/PhysRevC.93.035805

Time-of-flight mass measurements of neutron-rich chromium isotopes up to $N = 40$ and implications for the accreted neutron star crust

Z. Meisel,[1,2,*] S. George,[2,3] S. Ahn,[2,4] D. Bazin,[4] B.A. Brown,[4,5] J. Browne,[2,4,5] J.F. Carpino,[6] H. Chung,[6] R.H. Cyburt,[2,4] A. Estradé,[2,7] M. Famiano,[6] A. Gade,[4,5] C. Langer,[8] M. Matoš,[9] W. Mittig,[4,5] F. Montes,[2,4] D.J. Morrissey,[4,10] J. Pereira,[2,4] H. Schatz,[2,4,5] J. Schatz,[4] M. Scott,[4,5] D. Shapira,[11] K. Sieja,[12] K. Smith,[13] J. Stevens,[2,4,5] W. Tan,[1] O. Tarasov,[4] S. Towers,[6] K. Wimmer,[14] J.R. Winkelbauer,[4,5] J. Yurkon,[4] and R.G.T. Zegers[2,4,5]

[1] *Department of Physics, University of Notre Dame, Notre Dame, Indiana 46556, USA*
[2] *Joint Institute for Nuclear Astrophysics, Michigan State University, East Lansing, Michigan 48824, USA*
[3] *Max-Planck-Institut für Kernphysik, Heidelberg 69117, Germany*
[4] *National Superconducting Cyclotron Laboratory, Michigan State University, East Lansing, Michigan 48824, USA*
[5] *Department of Physics and Astronomy, Michigan State University, East Lansing, Michigan 48824, USA*
[6] *Department of Physics, Western Michigan University, Kalamazoo, Michigan 49008, USA*
[7] *Department of Physics, Central Michigan University, Mount Pleasant, Michigan 48859, USA*
[8] *Institute for Applied Physics, Goethe University Frankfurt a. M., Frankfurt a. M. 60438, Germany*
[9] *Physics Section, International Atomic Energy Agency, Vienna 1400, Austria*
[10] *Department of Chemistry, Michigan State University, East Lansing, Michigan 48824, USA*
[11] *Oak Ridge National Laboratory, Oak Ridge, Tennessee 37831, USA*
[12] *Université de Strasbourg, IPHC, CNRS, UMR7178, Strasbourg 67037, France*
[13] *Department of Physics and Astronomy, University of Tennessee, Knoxville, Tennessee 37996, USA*
[14] *Department of Physics, University of Tokyo, Hongo 7-3-1, Bunkyo-ku, Tokyo 113-0033, Japan*

We present the mass excesses of $^{59-64}$Cr, obtained from recent time-of-flight nuclear mass measurements at the National Superconducting Cyclotron Laboratory at Michigan State University. The mass of ^{64}Cr was determined for the first time with an atomic mass excess of $-33.48(44)$ MeV. We find a significantly different two-neutron separation energy S_{2n} trend for neutron-rich isotopes of chromium, removing the previously observed enhancement in binding at $N = 38$. Additionally, we extend the S_{2n} trend for chromium to $N = 40$, revealing behavior consistent with the previously identified island of inversion in this region. We compare our results to state-of-the-art shell-model calculations performed with a modified Lenzi-Nowacki-Poves-Sieja interaction in the fp-shell, including the $g_{9/2}$ and $d_{5/2}$ orbits for the neutron valence space. We employ our result for the mass of ^{64}Cr in accreted neutron star crust network calculations and find a reduction in the strength and depth of electron capture heating from the $A = 64$ isobaric chain, resulting in a cooler than expected accreted neutron star crust. This reduced heating is found to be due to the over 1 MeV reduction in binding for ^{64}Cr with respect to values from commonly used global mass models.

I. INTRODUCTION

The evolution of nuclear structure away from the valley of β-stability is a direct consequence of the forces at work in nuclei [1, 2]. Neutron-rich nuclides are of particular interest, since much of the neutron-rich nuclear landscape has yet to be explored [3]. Recently, the experimental reach of radioactive ion beam facilities has extended to chromium for neutron number $N = 40$, where an island of inversion has been inferred from various experimental signatures [4–9]. Trends in first 2^+ excited state energies $E(2_1^+)$ and ratios between first 4^+ excited state energies and $E(2_1^+)$ demonstrated a structural change between iron (proton number $Z = 26$) and chromium ($Z = 24$) isotopes near $N = 40$ [4, 5, 10, 11]. This increase in collectivity for chromium near $N = 40$, attributed to a rapid shape change from spherical to deformed structures, is further supported by quadrupole excitation strength $B(E2)$ measurements [6, 8, 9]. Nuclear mass measurements provide an independent probe of structural evolution which, in contrast to $B(E2)$ measurements, can avoid the bias to proton degrees of freedom [12, 13]. Precision mass measurements of manganese isotopes have indicated that the $N = 40$ sub-shell gap has broken down by $Z = 25$ [7]. However, mass measurements have yet to extend to $N = 40$ in the chromium isotopic chain.

The $N = 40$ chromium isotope ^{64}Cr is of astrophysical interest due to the expected prevalence of $A = 64$ material on the surfaces of accreting neutron stars, and therefore in the outer neutron star crust [14–16]. The trend in nuclear masses along an isobaric chain strongly impacts the depth and strength of electron capture reactions that heat and cool the outer crust, altering its thermal profile [17–19]. The resultant thermal profile impacts a host of astronomical observables, including the ignition of type-I x-ray bursts [20–22] and superbursts [23, 24], cooling of transiently accreting neutron stars while accretion is turned off [25, 26], and potentially gravitational wave emission [27, 28].

* zmeisel@nd.edu

To investigate the open questions in nuclear structure and astrophysics regarding the neutron-rich chromium isotopes, we performed time-of-flight (TOF) mass measurements of $^{59-64}$Cr ($Z = 24, N = 35 - 40$) at the National Superconducting Cyclotron Laboratory (NSCL) at Michigan State University. Argon and scandium mass measurements that were a part of the same experiment are discussed in Refs. [13] and [19], respectively. These new chromium masses show significant deviations from the chromium mass trend presented in the 2012 Atomic Mass Evaluation [29], implying a different structural evolution along the chromium isotopic chain. Our mass measurement of ^{64}Cr extends the mass trend of chromium out to $N = 40$ for the first time. We employ this ^{64}Cr mass in accreted neutron star crust reaction network calculations and, due to the reduction in binding of ^{64}Cr compared to global mass models, find less heating and shallower heating depths than previously expected.

II. EXPERIMENTAL SET-UP

A. Time-of-flight mass measurement technique

The masses presented in this work were measured via the time-of-flight (TOF) technique, in which the flight times of ions through a magnetic beam line system are converted to nuclear masses by comparison to the flight times of nuclides with known masses [30]. This technique was chosen due to its ability to obtain masses for exotic nuclides at the frontier of the known mass surface [18, 31]. We employed the TOF mass measurement set-up at the NSCL at Michigan State University described in detail in Ref. [32], shown in Fig. 1. This set-up consists of a 60.6 m flight path between the A1900 fragment separator [33] and S800 spectrograph [34], with fast-timing detectors located at the A1900 and S800 focal planes, magnetic rigidity $B\rho$ detection at the S800 target position, and energy loss and tracking detectors at the S800 focal plane [35]. About 150 neutron-rich isotopes of silicon to zinc were measured simultaneously over the course of ∼100 hours.

The Coupled Cyclotron Facility [36] at the NSCL was used to produce a 140 MeV/u ^{82}Se^{32+} primary beam with an intensity of ∼30 particle nA, which was fragmented on a beryllium target to produce nuclei of interest. Target thicknesses of 517 mg cm^{-2}, for production of less neutron-rich calibration nuclides, and 658 mg cm^{-2}, for production of more neutron-rich nuclides of interest were used alternately, keeping $B\rho$ of the A1900 and S800 fixed. Fragments were transmitted through the A1900 fragment separator [34], where slits reduced the momentum acceptance to ±0.5%. A 7.2 mg cm^{-2} Kapton wedge degrader was placed at the intermediate image of the A1900 to remove the high-flux of low-Z fragments that would have otherwise complicated particle identification (PID) and increased data acquisition dead-time. The S800 analysis line ion optics were set to a dispersion-matching mode to provide a momentum dispersion at the S800 target position of ≈1%/11 cm that enables an accurate rigidity measurement. This ion optical setting provides an achromatic focus on the timing detectors in the A1900 and S800 focal planes. The full set of nuclei detected over the course of the mass measurement is shown in Fig. 2. Timing and magnetic rigidity determinations will be discussed in more detail in Sections II B and II C, respectively.

The relationship between TOF and nuclear rest mass $m_{\rm rest}$ is obtained from the equation of motion for a charged massive particle through a magnetic system. Equating the two counteracting forces, the Lorentz force $F_{\rm L}$ and the centripetal force $F_{\rm c}$, results in the following relationship:

$$\begin{aligned} F_{\rm c} &= F_{\rm L} \\ \frac{\gamma(v) m_{\rm rest} v^2}{\rho} &= qvB \\ m_{\rm rest} &= \frac{1}{v}\frac{q(B\rho)}{\gamma(v)} \\ m_{\rm rest} &= \frac{\rm TOF}{L_{\rm path}}\frac{q(B\rho)}{\gamma\left(\frac{L_{\rm path}}{\rm TOF}\right)}, \end{aligned} \tag{1}$$

where the Lorentz factor γ is a function of velocity v, which is in turn the ratio of flight-path length $L_{\rm path}$ to flight time TOF. It follows that, in principle, the simultaneous measurement of an ion's TOF, charge q, and $B\rho$ through a system of known $L_{\rm path}$ yields $m_{\rm rest}$. However, in practice $L_{\rm path}$ and the ion optical dispersion used to measure $B\rho$ are not known with sufficient precision to obtain a precise value for $m_{\rm rest}$. Furthermore, it is more practical to make a relative than an absolute measurement of $B\rho$. Instead, the $\frac{m_{\rm rest}}{q}$ (TOF) relationship is determined empirically by measuring the TOF of calibration or reference nuclides [30]. The chosen reference nuclides have well-known masses ($\lesssim$ 100 keV uncertainty), no known isomers with lifetimes comparable to the flight time (∼500 ns), and are as close as possible in nuclear charge Z and mass A to the nuclides of interest in order to minimize systematic uncertainties [30].

Ultimately, TOF was measured for ∼150 nuclides, ranging from atomic number $14 \lessapprox Z \lessapprox 30$ and atomic mass to atomic number (here the ion charge $q = Z$) ratio $2.35 \lessapprox A/Z \lessapprox 2.72$. The measured TOFs were in the range of $\sim 500 \pm 25$ ns. The event-by-event TOFs were corrected for their $B\rho$ variation due to the finite $B\rho$ acceptance of the ion optical system using a globally-fit (i.e. fit over the full range of nuclides) correction based on the measured position at the S800 target location. The resultant single-species TOF distributions for the $B\rho$-corrected data were fit with a Gaussian distribution in order to determine a mean TOF for each nuclide. The relationship between mass over charge $m_{\rm rest}/q$ and TOF was fit to the data of reference nuclides in order to ascertain the calibrated $m_{\rm rest}/q$(TOF) relationship that was used to obtain the measured masses reported in this work.

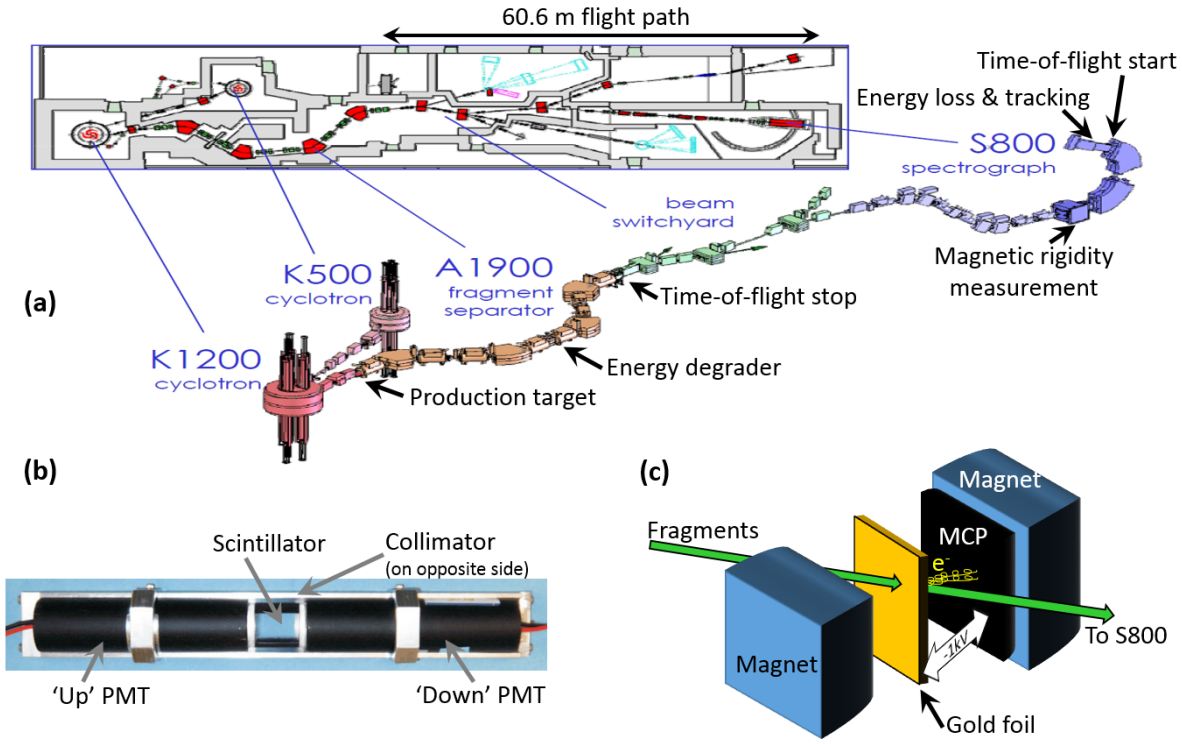

FIG. 1. (color online.) (a) Schematic of the NSCL time-of-flight (TOF) mass measurement set-up. (b) Scintillator and photomultiplier tube (PMT) pair used to measure TOF stop and start signals at the A1900 and S800 focal planes, respectively. Note that the delayed timing signal from the A1900 was chosen as the stop signal to avoid triggering on events which did not traverse the full flight path. (c) Schematic of the rigidity measurement set-up at the target position of the S800. The green arrow represents the beam fragments and the yellow spirals represent the secondary electrons fragments produce by passing through the gold foil, which follow a helical trajectory towards the microchannel plate detector (MCP) due to the -1 kV bias and magnetic field established by the permanent magnets.

B. Timing measurement

The method employed by Ref. [32] was used to measure the TOF for nuclides in the mass measurement reported here. Two 1 cm-tall×1.5 cm-wide×0.25 cm-thick BC-418 ultra-fast timing scintillators from Saint-Gobain Crystals [37] were each coupled to two Hamamatsu [38] R4998 1 in-diameter photomultiplier tubes (PMT) housed in a H6533 assembly (See Fig. 1b.). One timing detector was installed in the focal plane of the A1900 fragment separator, serving as the stop detector (after including a delay time). The second timing detector was installed in the focal plane of the S800 spectrograph. This choice for start and stop signals prevented triggering the data acquisition system for ions which did not traverse the full flight path. The signal from each PMT was split. One signal was used for timing information and the other signal was used to measure the magnitude of the light output for position and Z information. To maintain signal quality, timing signals were transported to the data acquisition electronics via Belden [39] model 7810A delay cables. This set-up provided an intrinsic timing resolution of ~ 30 ps [32].

Various combinations were made of the four PMT timing signals, one each from the 'Up' (low-$B\rho$ side) and 'Down' (high-$B\rho$ side) PMTs of the A1900 and S800 timing detector set-up, to create a TOF for each event, the 'event TOF', each of which is discussed in detail in Ref. [40]. The event TOF which was ultimately chosen to minimize the systematic uncertainty in the final results is the 'Down-Clock' TOF of Ref. [40]. For this event TOF, the high-$B\rho$ PMT signals from the S800 and A1900 fast-timing scintillators were each used to start separate channels of a time-to-amplitude converter (TAC), which each had a stop signal generated by a clock. Each separate TAC time randomly populated the full-range of an analog-to-digital converter (ADC), cancelling out systematic effects from local-nonlinearities in the ADC channel-to-time mapping that are difficult to characterize and correct. The random time-component of the event-TOF timing signals was removed by taking the difference between the two clock times, referred to as $T_{\mathrm{S3D-Clk}}$ and $T_{\mathrm{XFU-Clk}}$ for the S800 and A1900 low-$B\rho$-side PMT vs. clock times, respectively. The event TOF constructed from the clock-stopped time difference, $T_{\mathrm{XFD-Clk}} - T_{\mathrm{S3D-Clk}}$, for a given flight-time could vary by an integer multiple of the clock period ($T = 40$ ns), since the clock pulses came at random intervals with respect to the ion flight-time measurement. The event TOF

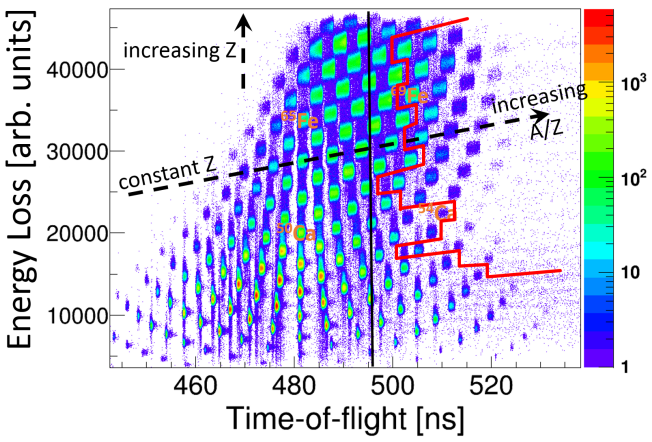

FIG. 2. (color online.) Particle identification plot of nuclei produced in this time-of-flight (TOF) mass-measurement experiment, where the color indicates production intensity (counts per 100 picoseconds×10 ionization-chamber-adc-units) and TOF was not rigidity-corrected. Nuclei located to the right of the red-line had no known experimental mass prior to the mass-measurement reported here; ^{50}Ca, ^{54}Ca, ^{65}Fe, and ^{69}Fe are labeled for reference. The data are from ≈ 11 hours of thin-target production and ≈ 91 hours of thick-target production.

was corrected for the number of clock pulses via a comparison to the direct time-of-flight measured between the two low-$B\rho$-side PMTs, as shown in Fig. 3. An additional correction was applied to each event-TOF to account for the systematic shift associated with an ion's scintillator impact-positions, which were obtained from the direct time-difference between the opposing PMTs on each of the fast-timing scintillators, $T_{\mathrm{XFU-XFD}}$ and $T_{\mathrm{S3U-S3D}}$.

The event-by-event TOF for each ion was

$$\begin{aligned}\mathrm{TOF}_{\mathrm{event}} &= T_{\mathrm{XFD-Clk}} - T_{\mathrm{S3D-Clk}} \\ &+ N_{\mathrm{d}}T + \frac{1}{2}(T_{\mathrm{XFU-XFD}} - T_{\mathrm{S3U-S3D}}) \\ &+ t_{\mathrm{offset}}, \end{aligned} \quad (2)$$

where N_{d} is the number of clock pulses to correct for (via Fig. 3) and t_{offset} =480 ns is an arbitrary offset applied to bring measured TOFs closer to the expected true TOFs, which differ due to the chosen delay-cable lengths.

C. Rigidity determination

A relative measurement of $B\rho$ was performed using the method developed by Ref. [41] at the target position of the S800 spectrograph, which was operated in a dispersion matched mode [34]. This consisted of sending the ion beam through a foil and guiding the secondary electrons generated in this process to the surface of an 8 cm-wide×10 cm-tall (where the width is along the non-dispersive direction) microchannel plate detector (MCP) (See Fig. 1.). The foil was a 70 μg cm^{-2} polypropylene film sputtered with 1500 Å of gold biased to −1 kV, which provided an electric field to guide electrons directly from the foil to the MCP, the face of which was at ground potential. The MCP consisted of two Quantar [42] model 3398A lead-glass plates oriented in the chevron configuration. Rectangular NdFeB 35 permanent magnets from Magnet Sales and Manufacturing [43] were held co-planar to the foil and MCP by a steel yoke in order to create a region of nearly homogeneous magnetic field between the foil and MCP, so that the secondary electrons would follow a tight spiral along their flight path. The secondary electrons were multiplied by the MCP in an avalanche which was collected on a resistive back plane, where electrons freely drifted to its four corners. The foil was mounted on a ladder which also contained a foil and hole-mask with a known hole pattern, shown in Fig. 4a, that was used for the dispersive position ($\propto B\rho$) calibration.

Ion impact positions on the MCP, and therefore on the foil, were reconstructed by determining the relative amount of charge collected on each corner of the resistive back plane. For a single event, the non-dispersive X_{MCP} and dispersive Y_{MCP} positions of an ion at the foil were given by

$$\begin{aligned} X_{\mathrm{MCP}} &= \frac{\mathrm{UR} + \mathrm{LR} - \mathrm{UL} - \mathrm{LL}}{\mathrm{UL} + \mathrm{UR} + \mathrm{LL} + \mathrm{LR}} \\ Y_{\mathrm{MCP}} &= \frac{\mathrm{UL} + \mathrm{UR} - \mathrm{LL} - \mathrm{LR}}{\mathrm{UL} + \mathrm{UR} + \mathrm{LL} + \mathrm{LR}}, \end{aligned} \quad (3)$$

where UL, UR, LL, and LR are the charges collected on the upper left, upper right, lower left, and lower right corners, respectively, of the MCP back plane. Each corner signal was split and sent through low and high-gain amplification, which were optimum for positions close to and far from a given corner, respectively. In practice, the positions reconstructed from the low-gain amplification were of comparable quality to the combined-gain positions, as seen in Fig. 4, and so the low-gain corner signals were used for the final MCP position determination. The achieved position resolution was $\sigma \approx 0.5$ mm and $\sigma \approx 1.0$ mm for secondary electrons generated by a ^{228}Th α-source and ^{82}Se primary beam, respectively, where the lower resolution for the primary beam was due to the larger initial kinetic energy of the secondary electrons [44], and therefore larger cyclotron radius [45, 46].

In addition to providing a relative measure of $B\rho$, the MCP position measurements were used to identify scattering on a collimator upstream of the foil that was used to protect the MCP during beam tuning. Scattering on the collimator reduced the energy of the scattered fragment, resulting in an increased energy loss in the S800 focal plane ionization chamber that was used for PID. These scattered events added a 'top-hat' feature above the 'main' (non-scattered) events in the PID, as shown in Fig. 5. A position gate, $X_{\mathrm{MCP}} < -11$ mm, was applied to remove scattered events from the analysis.

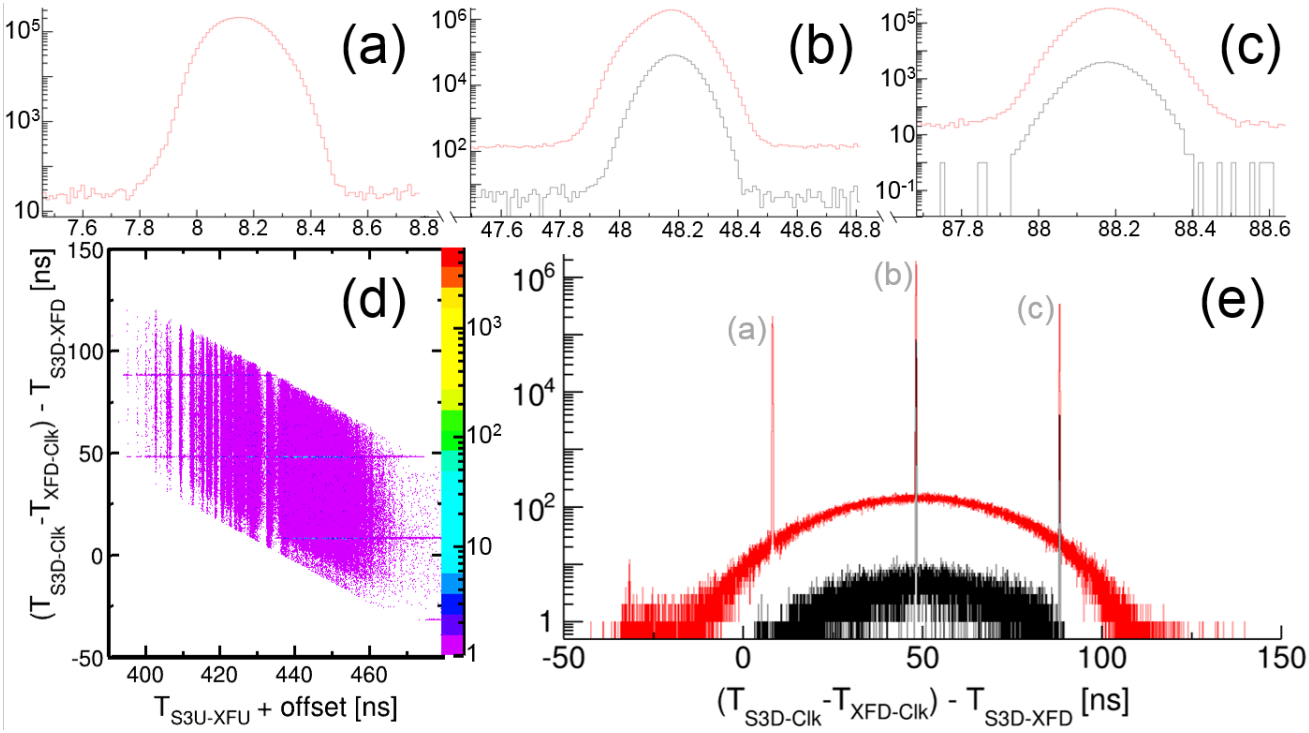

FIG. 3. (color online.) Spectra employed for the clock pulse correction. The time difference between a direct time-of-flight (TOF) and clock TOF (panel e), results in multiple peaks (panels a–c) spaced by the clock period T=40 ns. Narrow gates around the peaks were used to remove background and to determine the clock pulse correction that was to be added to a given event. Panel d demonstrates the fact that events of an ion with a single direct TOF could result in multiple clock TOFs. The random coincidences which are prominent in panel d are shown in panel e to be a small fraction of total events. The vertical structures in panel d are due to the fact that ions with similar A/Z had similar TOF, where the feature at $\approx$ 432 ns corresponds to $A/Z = 2.5$. The black histograms in panels a–c and e are gated on events of ^{45}Ar, the highest statistics isotope observed, while the red histograms are for all events.

III. DATA ANALYSIS

A. Rigidity correction

Due to the accepted momentum spread of $\pm 0.5\%$, a rigidity correction was required to remove the momentum-dependence from the measured TOF spectra. The $B\rho$ correction was first determined individually for each nuclide, the 'local' $B\rho$-correction, by fitting the TOF-Y_{MCP} relationship for the set of events belonging to a given nuclide. The parameters of the local rigidity corrections were then fit to determine a smooth variation of these parameters as a function of A and Z, resulting in the 'global' $B\rho$ correction which was ultimately used to momentum-correct the data. The global correction function allows for the momentum correction of nuclides with low statistics, for which a precisely determined local correction was not possible, removes spurious systematic effects from unphysical variations in the local rigidity corrections due to limited statistics, and its use for all nuclides ensures a consistent treatment of the data.

The local $B\rho$-correction was performed isotope-by-isotope in an iterative fashion. First, the TOF vs Y_{MCP} data for an isotope were histogrammed, converted into a graph with `ROOT`'s `TProfile` [47] class, and fit with a linear function (See Fig. 6). A linear function was chosen as it was found to reduce the overall systematic uncertainty in the final mass-fit [40]. The linear dependence of TOF on Y_{MCP} was then removed (See Fig. 6b), the data were projected onto the TOF dimension, and the projected histogram was fit with a normal distribution (See Fig. 6c). Due to contamination from misidentified nuclei in the PID, the TOF vs Y_{MCP} spectra contained two weak lines parallel to the main linear data trend, offset to higher and lower TOF, since low $B\rho$ (low TOF) events from higher-TOF nuclides could be misidentified as high $B\rho$ (high TOF) events from the nuclide of interest and vice versa for events from lower-TOF nuclides. The $B\rho$ measurement allowed these misidentified nuclei to readily be identified in the TOF vs Y_{MCP} spectra, however they skewed the slope of the initial linear fit. Therefore, following the fit-correction-projection-fit procedure shown in Fig. 6, a cut was made to only select events within 4σ from the TOF centroid of the normal distribution fit. The fit-correction-projection-fit procedure was then repeated until convergence was reached to obtain the slope

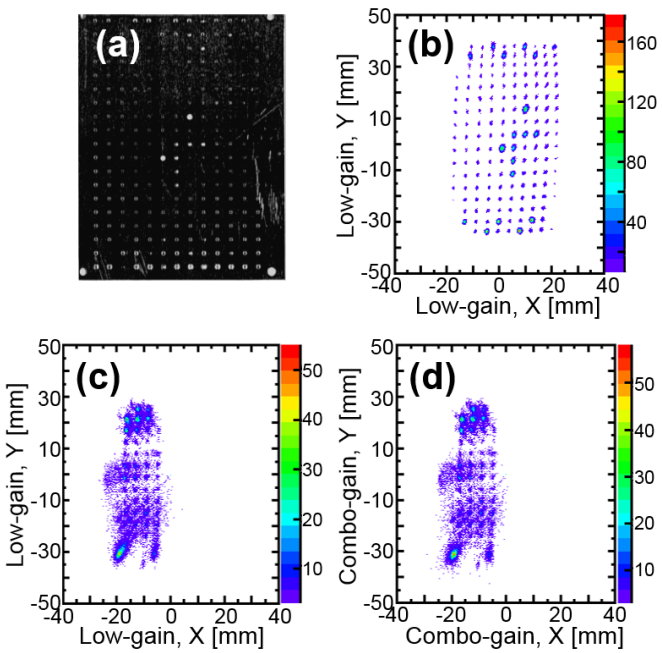

FIG. 4. (color online.) Panel (a) shows the mask with a distinctive hole pattern (5 mm hole-spacing) which was placed in between the incoming ion and gold foil in order to only allow electrons to be created from certain locations for calibration runs. Panel (b) shows the image created on the MCP by electrons generated from a ^{232}Th α-source. Panels (c) and (d) show the image created by the electrons generated by the ^{82}Se primary beam, where the beam was tuned to four separate positions to achieve the mask-coverage shown, where the low-gain corner signals were used for panel (c) and the combined high-low gain signals were used for panel (d). Since only the relative position was relevant, the effort was not made to achieve the exact 5 mm hole-spacing of the mask in the MCP image.

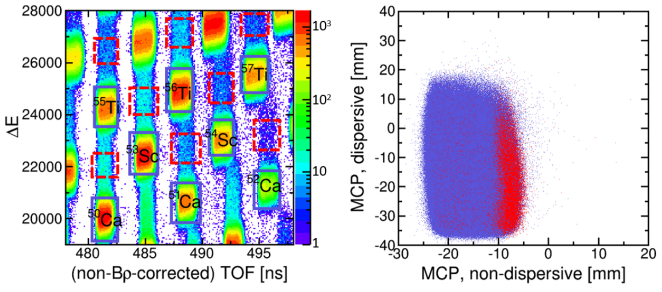

FIG. 5. (color online.) Demonstration of the correlation between high energy-loss (ΔE) PID events and the microchannel plate (MCP) non-dispersive position. The left panel shows a subset of the PID containing isotopes of calcium, scandium, and titanium, where 'main' events are within the purple boxes and 'top-hat' events are within the red-dashed boxes. The right panel shows the location of the 'main' (purple dots) and 'top-hat' (red dots) events on the MCP, where it is clear that the relatively high ΔE events corresponded to larger non-dispersive positions.

of the local $B\rho$-correction for that isotope. The linear local $B\rho$-correction was found to be insufficient for isotopes of elements with $Z < 17$ and $Z > 26$ and nuclides with $A/Z < 2.44$, so these nuclides were excluded from the analysis. On average the slope of the TOF–$Y_{\rm MCP}$ relationship was ~ 40 ns mm^{-1}.

The locally determined linear dependencies of TOF on $Y_{\rm MCP}$ were then fit to determine a global $B\rho$-correction. Various polynomials in A, Z, and A/Z were explored, up to fourth order in each variable, and the optimum fit-function in terms of goodness of fit was selected:

$$\left(\frac{d\mathrm{TOF}}{dY_{\rm MCP}}\right)_{\rm global} = a_0 + a_1\frac{A}{Z} + a_2\left(\frac{A}{Z}\right)^2 + a_3 Z + a_4 Z^2 + a_5 A, \quad (4)$$

where a_i are fit parameters. The global $B\rho$-correction slopes from this fit reproduced the local $B\rho$ correction slopes within 1%. The same optimum global fit function was found by Ref. [18]. An element-by-element fit to the local $B\rho$-correction slopes was also explored, though it was found to be inferior in terms of the final mass-fit systematic uncertainty [40]. The local, global, and by-element $B\rho$-correction slopes are compared in Fig. 7. Note that isotopes with $Z = 17$ are not shown since they were ultimately excluded from the analysis due to their drastically different behavior in TOF as a function of m/q, as determined by the mass-fit (Recall isotopes of elements with $Z < 17$ and $Z > 26$ were previously excluded from the analysis due to their poor local $B\rho$ correction determination.).

The global $B\rho$-correction was applied to the TOF spectra, as is shown in Fig. 8 for the chromium isotopes, where it is apparent that a shift in the average TOF of the distribution occurs due to the choice of $Y_{\rm MCP}$ which TOF was pivoted about. The $B\rho$-correction improved $\sigma_{\rm TOF}$ from $\sim$2 ns to $\sim$0.08 ns. The final TOF for each nuclide was determined by fitting the $B\rho$-corrected TOF with a normal distribution, gating on events within $\pm 4\sigma$ of the TOF centroid, and repeating the fitting-gating procedure until convergence. The statistical uncertainty of the mean TOF for measured nuclides was $\delta\mathrm{TOF} \lesssim 1$ ps, corresponding to a TOF measurement precision of roughly one part in 10^6.

B. Mass evaluation

The fit to the mass over charge m/q–TOF surface, elsewhere referred to in this article as the 'mass-fit', consisted of choosing a set of reference nuclides to calibrate the $m_{\rm rest}/q$(TOF) relationship, finding the optimum fit function, and assessing the various uncertainties contributing to the final mass results obtained for nuclides that were not used as calibrants. Nuclides chosen as calibrants had a literature experimental mass uncertainty ≤ 50 keV, as listed in the 2012 Atomic Mass Evaluation [29] (except for ^{53}Ca and ^{54}Ca which come from Ref. [48]), and no

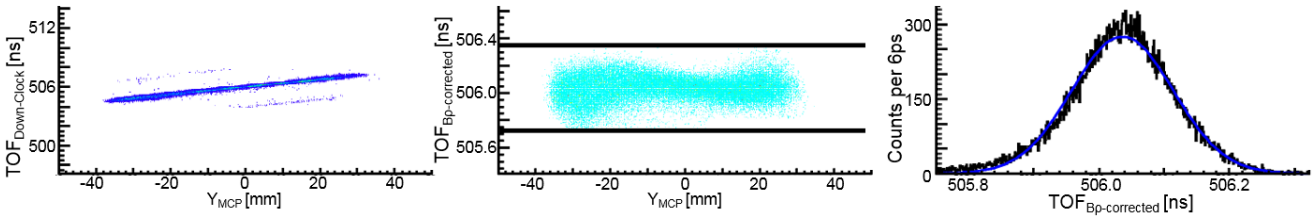

FIG. 6. (color online.) The first iteration of the local $B\rho$-correction for ^{64}Cr. The left panel shows a histogram of TOF vs Y_{MCP} for events identified as ^{64}Cr, which was converted to a graph by applying ROOT's TProfile class to the histogram and fit with a linear function. The middle panel shows the resultant $B\rho$-corrected TOF vs Y_{MCP} histogram after removing the linear trend found in the left panel, pivoting about Y_{MCP}=0. The right panel shows the projection onto the TOF-dimension of the rigidity corrected (black histogram) TOF vs Y_{MCP} relationship, where the blue line is a Gaussian fit. The black lines in the middle panel indicate $\pm 4\sigma$, where σ is the standard deviation of the Gaussian fit of the right panel.

isomers longer-lived than 100 ns, as listed in the National Nuclear Data Center database [49]. The twenty nuclides used to calibrate the m_{rest}/q(TOF) relationship were $^{44-47}$Ar, $^{47-51}$K, $^{49-54}$Ca, ^{63,65,66}Mn, and ^{64,66}Fe. A map of the reference nuclides with respect to the nuclides for which a mass was evaluated is shown in Fig. 9.

The atomic masses from Ref. [29] were corrected to obtain nuclear masses by subtracting the individual electron binding energies listed in Table II of Ref. [50]. A relativistic correction was applied to the measured TOF for nuclides in order to account for time-dilation. Additionally, the average TOF and Z for all nuclides of interest were subtracted from the TOF and Z of each nuclide to create effective time and charge variables, i.e. $\tau = \mathrm{TOF} - \langle \mathrm{TOF} \rangle$ and $z = Z - \langle Z \rangle$, in order to reduce the multicollinearity of the mass-fit parameters [32].

The initial uncertainty in m_{rest}/q ascribed to the data points was the literature mass uncertainty added in quadrature to the statistical uncertainty, where the latter used standard propagation of uncertainty to translate uncertainty in TOF into uncertainty in m/q. This statistical uncertainty depended on the fit function itself, $\delta M_{\mathrm{stat.}} = (\delta\mathrm{TOF}) \times \frac{\partial}{\partial \mathrm{TOF}} \left(\frac{m}{q}(\mathrm{TOF}) \right)$ where $\frac{m}{q}$(TOF) is the m_{rest}/q(TOF) calibration function and δTOF is the one standard deviation uncertainty of the mean TOF for a nuclide (data point). Therefore, the final statistical uncertainty assigned to each data point was determined in an iterative procedure where the data was fit to obtain a m_{rest}/q(TOF) calibration function, statistical uncertainties were calculated for each of the data-points (corresponding to reference nuclides), and the process was repeated until convergence.

Upon completion of the mass-fit, including literature and statistical uncertainties, the reduced χ^2 of the fit was typically much larger than one. This indicated that the uncertainty of the twenty reference nuclide data-points was underestimated and that some additional heretofore unaccounted for uncertainty was present. As there were no systematic trends in the fit residuals, we treat the additional uncertainty as a systematic error. The approach outlined in [32] was followed, where the missing uncertainty was treated as a statistically-distributed systematic uncertainty, i.e. one that accounted for a uniform scatter in the mass-fit residual as a function of m_{rest}/q (We note that a similar procedure has been used previously in storage ring isochronous mass spectrometry [51].). Such an effect could have been created by many uncontrolled factors in the measurement, such as time-dependent magnetic field drift of the dipole magnets along the beam line, time-dependent variations in the response of the timing electronics due to variations in temperature, or unidentified biases present in the data analysis pipeline. To include this additional systematic uncertainty, the uncertainty of reference nuclide data-points was increased uniformly, i.e. each data point had the same systematic uncertainty $\delta M_{\mathrm{syst.}}$ (in keV q^{-1}), until $\chi^2_{\mathrm{red.}} = 1$. We note that the results of the mass-fit with and without inclusion of the systematic uncertainty agreed within the final one standard deviation uncertainty. The mass-fit was then repeated and the statistical uncertainty was recalculated to be consistent with the current parameters of the fit function. This process was then repeated iteratively until it converged. The fit-function resulting from this procedure was the m_{rest}/q(TOF) calibration function which was used to obtain masses for non-calibration nuclides whose TOF was measured.

Since the relationship between mass and TOF at the precision level required to make a meaningful mass measurement was a priori unknown, several fit functions were tried, each of which was a combination of polynomials in TOF, nuclear charge Z, and/or a combination of these variables. The goal of this approach was to find the minimum number of terms that reproduce the calibration mass surface without any systematic trends in the fit residuals. This ensures maximum robustness against interpolation and small-distance extrapolation. The complex nature of the m_{rest}/q–TOF surface (See Fig. 10.) clearly necessitated higher orders in both TOF and Z. A step-by-step procedure was taken to justify the inclusion of each term added to the mass-fit function. To be included in the fit function, an extra term had to significantly reduce the fit residuals and not introduce any

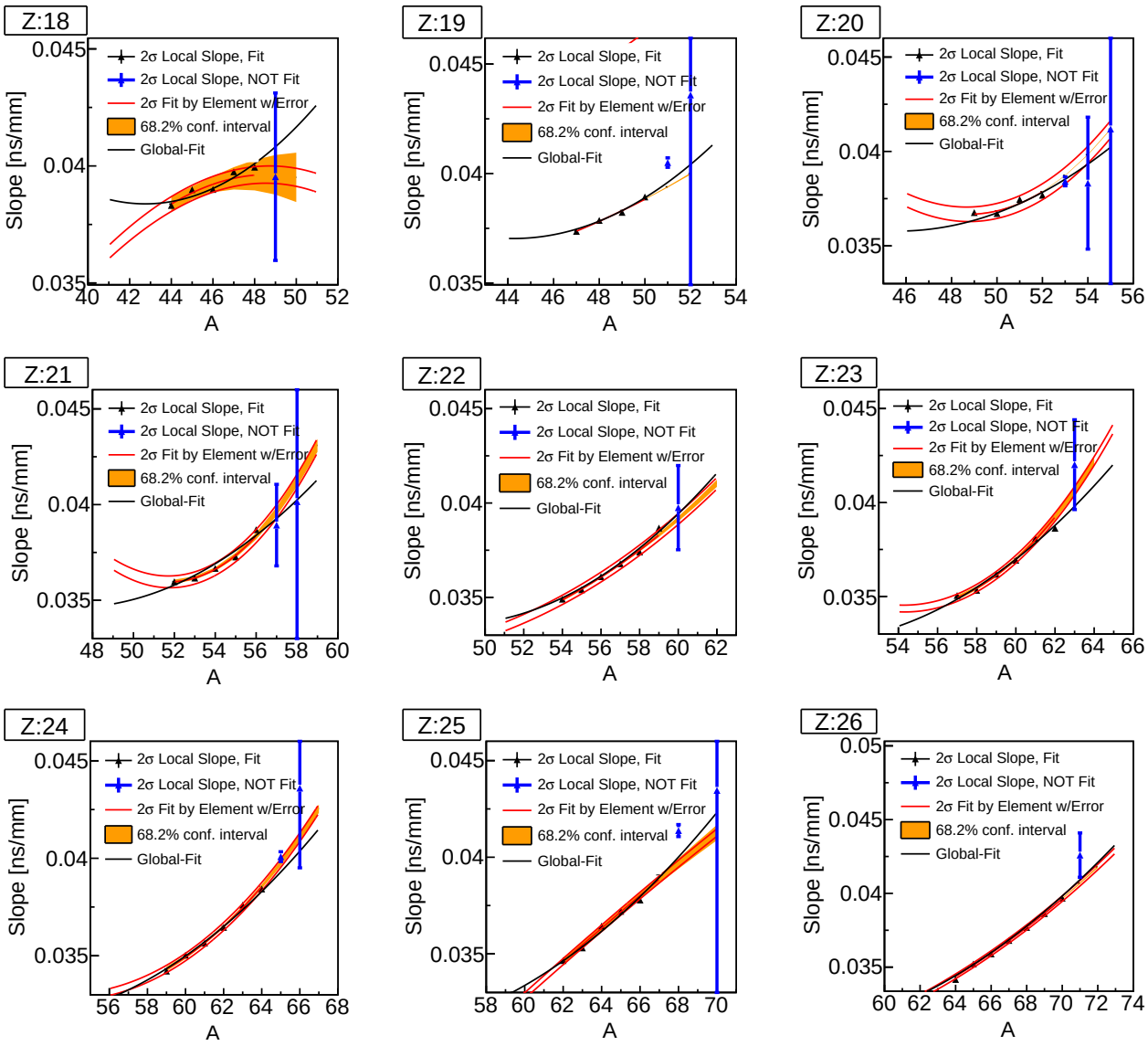

FIG. 7. (color online.) TOF vs $Y_{\rm MCP}$ slope as a function of mass number A for observed isotopes of argon, potassium, calcium, scandium, titanium, vanadium, chromium, manganese, and iron ($18 \leq Z \leq 26$), respectively, as determined by 'local' by-nucleus fits (data points) and fits to the locally-determined slopes that employed the $\pm 2\sigma$ cut-off, where the black data points were included in the fit and the blue points were not. The by-element fit along a single isotopic chain as a cubic function of A is shown by the red lines, where the upper and lower lines indicate the extremes obtained for upper and lower limits of the fit-parameters, and the orange band indicates the $\pm 1\sigma$ confidence interval. The black line shows the trend of the rigidity-correction slope along an isotopic chain as determined by the global fit to all locally-determined slopes of nuclei with $A/Z > 2.44$ and $18 \leq Z \leq 26$.

systematic trends. The final mass-fit function which was chosen represents the minimal set of terms that minimizes the overall residual to literature masses of the twenty reference nuclides and resulted in no detectable systematic biases (i.e. trends in the mass-fit residuals). As might be expected, some degeneracy existed as to the benefit of including certain terms in the fit-function. This set of 'best' fits was used to inform the uncertainty of masses evaluated from the mass-fit function present from extrapolation-from and interpolation-between the mass-fit calibration points (See Section III C.).

The final mass-fit function employed for the mass results was

$$\frac{m}{q}(\tau) = a_0 + a_1\tau + a_2 z + a_3\tau^2 + a_4 z^2 + a_5 z\tau + a_6 z^4, \quad (5)$$

where a_i are fit parameters. The optimum mass-fit function (of the set explored) and the mass results obtained with Eqn. 5 were found to be robust with respect to the removal of a subset of reference nuclides from the mass-fit [40]. Fig. 10 shows Eqn. 5 fit to the $m_{\rm rest}/q$(TOF)

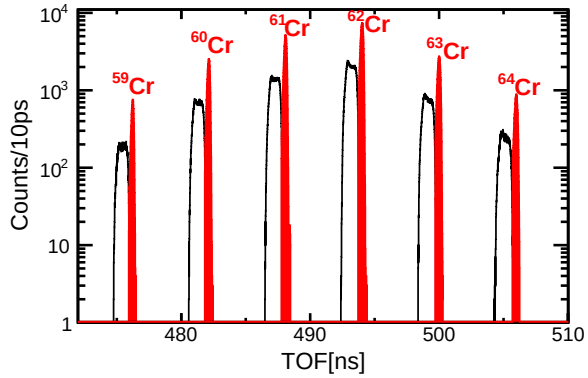

FIG. 8. (color online). Time-of-flight (TOF) distribution of chromium isotopes before (open histograms) and after (red-filled histograms) the global magnetic rigidity correction.

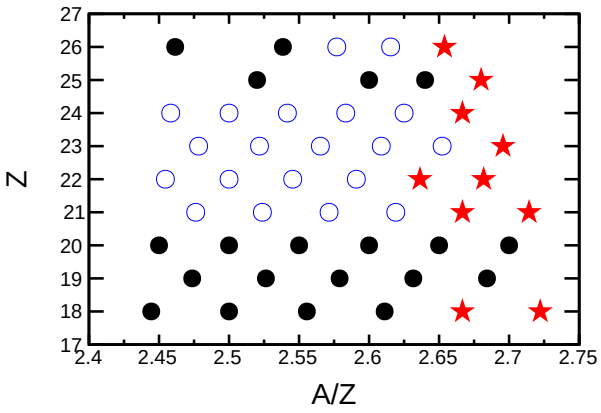

FIG. 9. (color online.) Map of nuclides observed in the TOF mass measurement (with sufficient statistics to obtain a TOF value) in terms of atomic mass number to nuclear charge ratio A/Z and nuclear charge Z. Solid black circles indicate reference nuclides, open blue circles indicate nuclides with masses known in the literature, but not to sufficient precision to qualify as reference nuclides, and red stars indicate nuclides with unknown mass prior to this experiment. The isotopes ^{63}Mn and ^{63,65}Fe were not considered, as they have known low-lying isomers that preclude these nuclides as calibrants of the mass fit. Our results for $Z = 18$ and $Z = 21$ are published in Refs. [13] and [19], respectively. Our results for $Z = 25, 26$ will be the subject of a forthcoming publication.

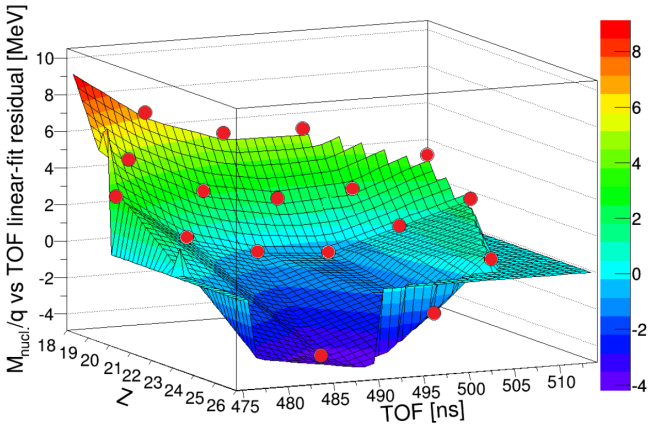

FIG. 10. (color online.) $m_{\rm rest}/q$–TOF surface of reference nuclides where the linear dependence of mass over charge m/q on TOF has been removed. Solid red points mark the nuclear charge Z and TOF of reference nuclides while the color of the surface at that location indicates the linear fit residual in MeV. (Note that the flat region that is present outside of the region bounded by data points is a feature of the plotting software.)

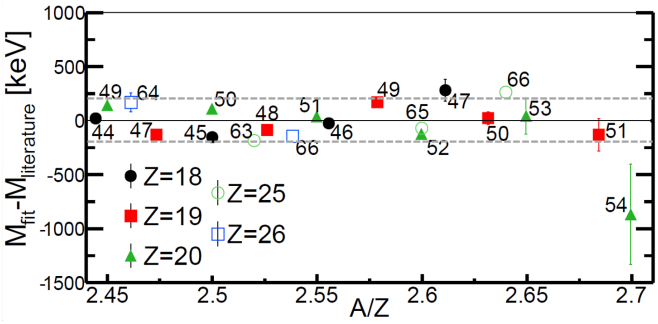

FIG. 11. (color online.) Residuals of the fit to the m/q(TOF) relationship of calibration nuclides ($^{44-47}$Ar, $^{47-51}$K, $^{49-54}$Ca, ^{63,65,66}Mn, and ^{64,66}Fe) as a function of the mass number to nuclear charge ratio A/Z. Error bars indicate statistical uncertainties only. The horizontal dashed-gray lines indicate the average systematic mass uncertainty (9 keV/q) included for reference nuclides for the mass fit, as described in Section III B.

data for calibration nuclides. The mass-fit residuals for Eqn. 5 are shown in Fig. 11.

Eqn. 5 contains one extra term, $z\tau$, and favors z^4 over z^3 behavior with respect to the previous TOF mass measurement at the NSCL [18]. The z^4 term is only slightly favored over the z^3 term, and a function using the z^3 term instead is included in the set of best-fit functions used to evaluate the extrapolation uncertainty (See Section III C.). We surmise that the inclusion of the $z\tau$ term is required due to the extra energy loss induced by the wedge degrader at the intermediate image of the A1900, which was not present in Ref. [18]. This is because $z\tau \propto A$ and, for fixed $B\rho$, energy loss $\Delta E \propto A$ (since $\Delta E \propto Z^2/E$, $E \propto Av^2$, and $(B\rho)^2 = (p/q)^2 \propto ((Av)/Z)^2$ =constant, where v is the ion velocity and $q = Z$ for the fully-stripped ions measured here).

C. Measurement uncertainty

The mass uncertainty for measured nuclides which were not reference nuclides was comprised of a statistical uncertainty determined from the nuclide's individual count rate, the statistically-distributed systematic uncertainty which was determined to be present for reference nuclides (and therefore assumed to be present for evaluated nuclides), and two additional uncertainties were included to account for the uncertainty in the mass-fit function. Namely, these were the uncertainties of the fit coefficients that were a result of the uncertainties in the calibration mass values and TOFs, referred to here as the 'Monte Carlo' uncertainty (motivated by the way it was calculated), and the uncertainty from the choice of the general form of the fit function, referred to here as the 'function choice' uncertainty.

For the Monte Carlo uncertainty assessment, the mass of each reference nuclide was perturbed by a random amount commensurate with its uncertainty, the mass-fit was performed, the fit results were recorded in a histogram, and this perturbation-fit-histogram procedure was repeated 10,000 times. The Monte Carlo uncertainties are the standard deviations of the fit-result mass distributions.

The function choice uncertainty was defined as the difference between the highest and lowest mass value for a given nuclide resulting from the set of mass-fits that were explored which required a systematic uncertainty less than three times that of the best mass-fit to produce a reduced χ^2 equal to one and showed no systematic trend in mass-fit residuals. The five fits with six, seven, or eight parameters which were considered for the function choice uncertainty were Eqn. 5 and similar functions which contained a z^3 term rather than a z^4 term, lacked the a_6 term altogether, included an additional term that depended on τ^4, and included an additional term that instead depended on $z^*\tau^2$. The required statistically-distributed systematic uncertainty required for each of these fit functions was 9.0 keV/q, 11.2 keV/q, 22.7 keV/q, 8.5 keV/q, and 8.2 keV/q. Note that the eight-parameter mass-fit functions were not used in lieu of Eqn. 5 as they did not yield a significant reduction in the required systematic uncertainty and thus did not contain the minimal set of terms required to minimize the overall residual to literature masses of the reference nuclides.

Fig. 12 shows the statistical (a), systematic (b), Monte Carlo (c), and function choice (d) uncertainties of the masses evaluated in this experiment. Their sum in quadrature is shown in Fig. 13. It is apparent that the relative contribution of the uncertainties resulting from the mass-fit extrapolation and interpolation, i.e. the Monte Carlo and function choice uncertainties, becomes larger as the distance in m/q and Z from reference nuclides increases. For the chromium isotopes, which are the focus of this work, the function choice uncertainty dominates, as the Z-dependence of the $m_{\rm rest}/q$(TOF) relationship is poorly constrained by the available reference nuclides. New high-precision mass measurements of neutron-rich isotopes of scandium and vanadium would improve this situation.

IV. RESULTS

The atomic mass excesses for the chromium isotopes measured in this experiment are compared to theoretical and literature values in Tab. I, where we note that the mass of ^{64}Cr was measured for the first time. These results correspond to a mass measurement precision of roughly one part in 10^5.

For our mass comparison in Tab. I we focus on previous experimental values reported [52–54] by the Time-of-flight Isochronous Spectrometer (TOFI) facility, as these results constitute the primary contribution to the evaluated mass reported for these isotopes in the 2012 Atomic Mass Evaluation (AME) [29]. We compare to the theoretical results reported by the 1995 Finite Range Droplet Model (FRDM) [55] and Hartree-Fock-Bogoliubov-21 (HFB-21) [56] since these models are commonly used in astrophysics calculations when experimental data are not available (e.g. Refs. [17, 18, 57, 58]). Additionally, we compare our mass-differences to those calculated via the shell-model using different interactions and model spaces.

Fig. 14 compares the trend in two-neutron separation energy S_{2n}, $S_{2n}(Z,A) = 2\times \mathrm{ME}_{\rm neutron} + \mathrm{ME(Z, A-2)} - \mathrm{ME(Z, A)}$, for neutron-rich isotopes of chromium determined from masses reported in this work to the trends obtained for masses from the 2012 AME [29] and binding energies calculated by the shell-model employing the GXPF1A Hamiltonian [59] in the fp-shell model space, as well as shell-model calculations employing a modified version of the Hamiltonian from Ref. [11], which is discussed further in the following section. We note that we extend the S_{2n} trend for the chromium isotopes to $N = 40$ for the first time. The energies of the yrast 2^+ excited states are included in Fig. 14 for comparison, as this trend conveys similar information regarding the evolution of nuclear structure along the chromium isotopic chain [13].

The discrepancies in experimentally-based S_{2n} values, which are largest at $N = 36$ and $N = 38$, primarily stem from the $\sim$ 650 keV, $\sim$ 950 keV, and $\sim$ 600 keV differences between this work and the AME values for ^{59}Cr, ^{60}Cr, and ^{61}Cr, respectively. In particular, the difference between our ^{60}Cr mass excess and the adopted AME value causes the S_{2n} trend for $N = 36-38$ to pivot about $N = 37$. As seen in Tab. I of Ref. [29], the 2012 AME values for these three nuclides are primarily based on three separate measurements from the TOFI facility [52–54], amongst which there is a $\sim$ 500 keV discrepancy for the reported masses of ^{59,60}Cr and a $\sim$ 1700 keV discrepancy for the reported ^{61}Cr masses (See Tab. I.).

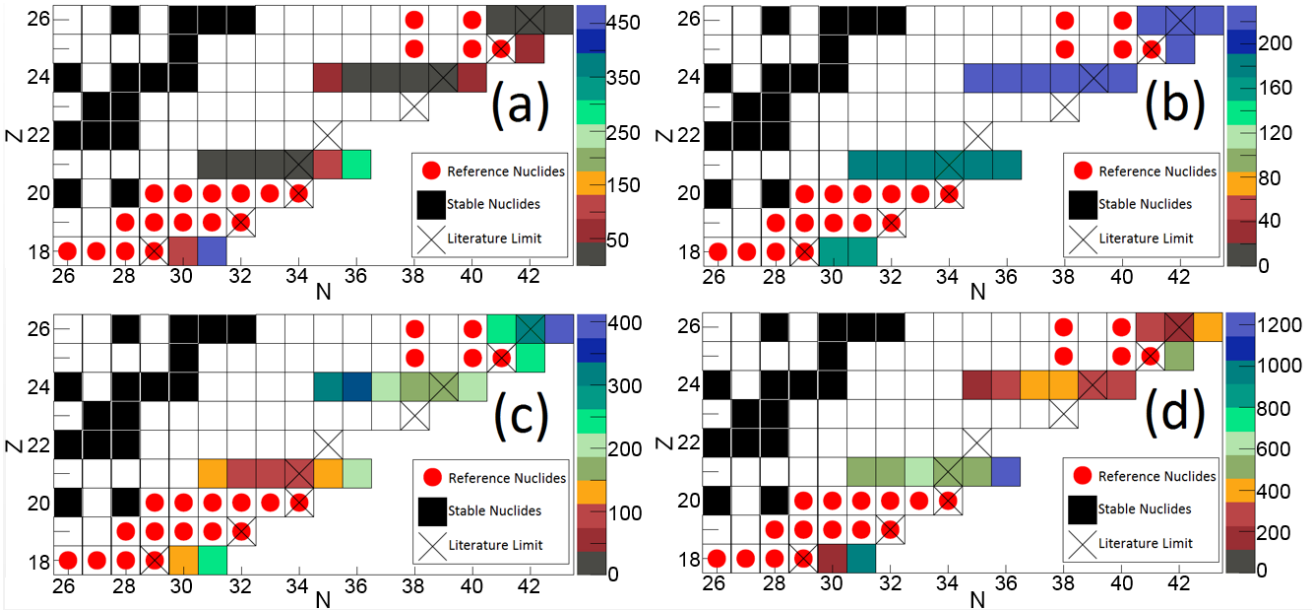

FIG. 12. (color online.) Statistical (a), systematic (b), Monte Carlo (c), and function choice (d) uncertainties in keV for nuclides whose mass was evaluated in this time-of-flight mass measurement. Colored boxes indicate nuclides whose mass was evaluated, with the color reflecting the uncertainty in keV, boxes with red circles indicate reference nuclides used as calibrants for the $m_{\rm rest}/q$(TOF) relationship, boxes with $\times$'s indicate the most exotic isotope for that element with a known mass prior to this experiment, and the black boxes indicate stable nuclides.

TABLE I. Atomic mass excesses (in keV) of chromium isotopes measured in this experiment compared to results from previous direct mass measurements from the Time-of-flight Isochronous (TOFI) spectrometer (TOFI1 [52], TOFI2 [53], and TOFI3 [54]), the adopted value in the 2012 Atomic Mass Evaluation (AME) [29] ('E' are extrapolations), and predictions from global mass models (FRDM [55] and HFB-21 [56]).

Isotope	This experiment	AME 2012	TOFI1	TOFI2	TOFI3	FRDM	HFB-21
^{59}Cr	−48 540 (440)	−47 891 (244)	−47 710 (230)	−47 850 (250)	−47 320 (310)	−48 680	−49 160
^{60}Cr	−47 440 (460)	−46 504 (213)	−46 280 (230)	−46 830 (260)	−46 510 (280)	−47 910	−48 200
^{61}Cr	−43 080 (510)	−42 455 (129)	−41 500 (400)	−42 770 (280)	−42 120 (280)	−42 700	−43 710
^{62}Cr	−40 890 (490)	−40 895 (148)	−39 500 (600)	−41 200 (400)	−40 200 (350)	−41 180	−41 960
^{63}Cr	−35 940 (430)	−35 722 (459)	...	...	...	−36 030	−37 290
^{64}Cr	−33 480 (440)	−33 459E (298E)	...	...	...	−34 950	−34 730

V. DISCUSSION

A. Structural evolution of the neutron-rich chromium isotopes

The trend in binding energies determined in this work can be used as a probe of the evolution of shell structure for neutron-rich chromium isotopes [12]. Typically, S_{2n} is employed to isolate the structural changes present along neutron-rich isotopes of an element (e.g. Refs. [7, 13, 31, 48, 63]). Along an isotopic chain, S_{2n} generally declines with increasing N away from β-stability due to the penalty in binding energy for a large neutron-proton asymmetry, as described by the liquid-drop model. This decline is markedly increased following a nucleus that exhibits a magic neutron number, since the two-neutron removal (addition) required to move from (to) a nucleus with magic N is energetically disfavored (favored) due to the shell-gap associated with $N_{\rm magic}$ [12]. A leveling of S_{2n} for a few isotopes, followed by a continuation of the gradually decreasing trend is a signature of a shape transition along an isotopic chain [64].

The S_{2n} trends in Fig. 14 demonstrate the different structural changes implied by the masses presented in this work and the evaluated masses of the 2012 AME [29]. Our new data disfavors the change in the S_{2n} slope at $N = 36$ shown by the 2012 AME data, instead favoring a continuation of the previous slope until $N = 38$. We note that the flattening of the AME S_{2n} trend about $N = 36$ is more consistent with the identification of ^{60}Cr

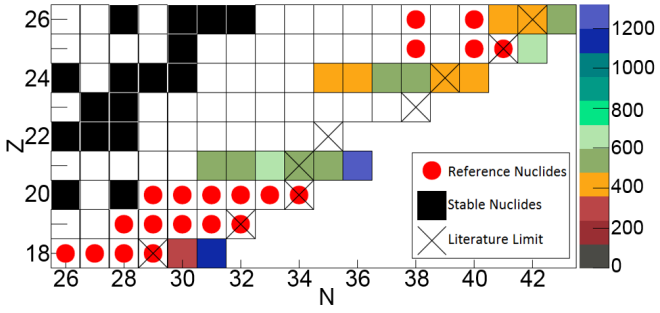

FIG. 13. (color online.) Same as panels in Fig. 12, but with the color indicating the total uncertainty of evaluated nuclide in keV, where the total is the sum in quadrature of the statistical, systematic, Monte Carlo, and function choice uncertainties. Note that ^{56}Sc has an additional systematic uncertainty due to the presence of a β-decaying isomer (See Ref. [19] for more detail.) which is not included in this figure.

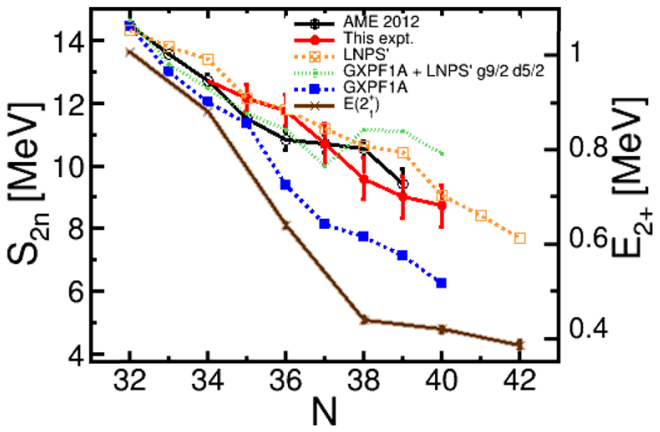

FIG. 14. (color online.) Two-neutron separation energy S_{2n} for neutron-rich isotopes of chromium as calculated from the 2012 Atomic Mass Evaluation (open black circles) and the masses reported here (solid red circles), as well as calculated by shell-model calculations employing the GXPF1A Hamiltonian [59](solid blue triangles) and LNPS' Hamiltonian (modified from Ref. [11]) (open orange squares). The contribution of the $g_{9/2}$ and $d_{5/2}$ orbitals is shown by adding their contribution to the LNPS' results to S_{2n} calculated with the GXPF1A Hamiltonian (green points). The energies of yrast 2^+ excited states of corresponding isotopes are shown for comparison (brown crosses) [5, 60–62].

as the shape-transition point by Ref. [9]. The decrease in the magnitude of our S_{2n}-trend slope approaching $N = 40$ is consistent with the collective behavior previously identified by Refs. [5–9]. It is interesting to note that our S_{2n} trend for $^{62-64}$Cr ($N = 38 - 40$) resembles the trend for $^{30-32}$Mg [65] ($N = 18 - 20$), where ^{32}Mg marks the entrance of the magnesium isotopic chain into the $N = 20$ island of inversion [66–68]. However, the masses of chromium isotopes with $N > 40$ are required to provide a firm signature of the presence or absence of the $N = 40$ sub-shell gap for this element.

The striking divergence between the experimental S_{2n} trends and the shell-model derived trend (GXPF1A) shown in Fig. 14 highlights the need for inclusion of the $g_{9/2}$ and $d_{5/2}$ orbits in order to obtain a realistic description of the chromium isotopes for $N \geq 35$, which has been pointed-out by previous studies [69–71]. We have thus performed large scale shell-model calculations within the proton fp and neutron $fpg_{9/2}d_{5/2}$ model space, employing the Hamiltonian from Ref. [11] with minor modifications [72, 73]. Additionally, the global monopole term was made more attractive by 30 keV to obtain a better agreement of the S_{2n} energies in neutron-rich chromium and iron isotopes. These refinements preserve the spectroscopy of the nuclides in the island of inversion region presented previously in Ref. [11].

The results of the calculations with the modified LNPS Hamiltonian, dubbed hereafter LNPS', are also presented in Fig. 14. As can be seen, the agreement is more satisfactory than for the GXPF1A Hamiltonian and the LNPS' results match with the present data within the error bars for the majority of cases. The largest discrepancy is found for the S_{2n} value of ^{63}Cr, which is overestimated. This is surprising as the present model accurately reproduces the known excitation energies of chromium isotopes, with the visible drop of the yrast 2^+ excited state energies between $N = 36$ and $N = 38$, indicating that chromium isotopes undergo a shape change at $N = 38$. However, little is known about the spectroscopy of ^{63}Cr [74] and the ground-state spin assignments of both ^{63}Cr and ^{61}Cr are tentative, making it difficult to evaluate whether these nuclides have the correct degree of collectivity in the present shell-model calculations. In spite of this discrepancy, the LNPS' shell-model trend points clearly to the development of collectivity around $N = 40$ and predicts continuation of the deformation onset towards higher neutron numbers. This increase in collectivity agrees with the recent measurement of the yrast 2^+ excited state energy for ^{66}Cr [62].

We have also examined the summed occupancies of the neutron intruder orbitals $g_{9/2}$ and $d_{5/2}$ within the LNPS' model. The contribution of those is shown in Fig. 14, added to the GXPF1A results. The occupation of the neutron intruder orbitals becomes significant at $N = 36$ (∼1.8 particles) and coincides directly with the place where the deviation between GXPF1A calculations and experiment becomes large. Further increase of this occupancy with increasing neutron number (see also Tab. II of Ref. [11]) explains the failure of shell-model calculations limited to the fp-shell model-space to reproduce S_{2n} for the neutron-rich chromium isotopes.

B. $A = 64$ electron capture heating in the accreted neutron star crust

Heating and cooling due to electron capture reactions within the accreted neutron star crust have been shown to affect the outer crust thermal profile and the associ-

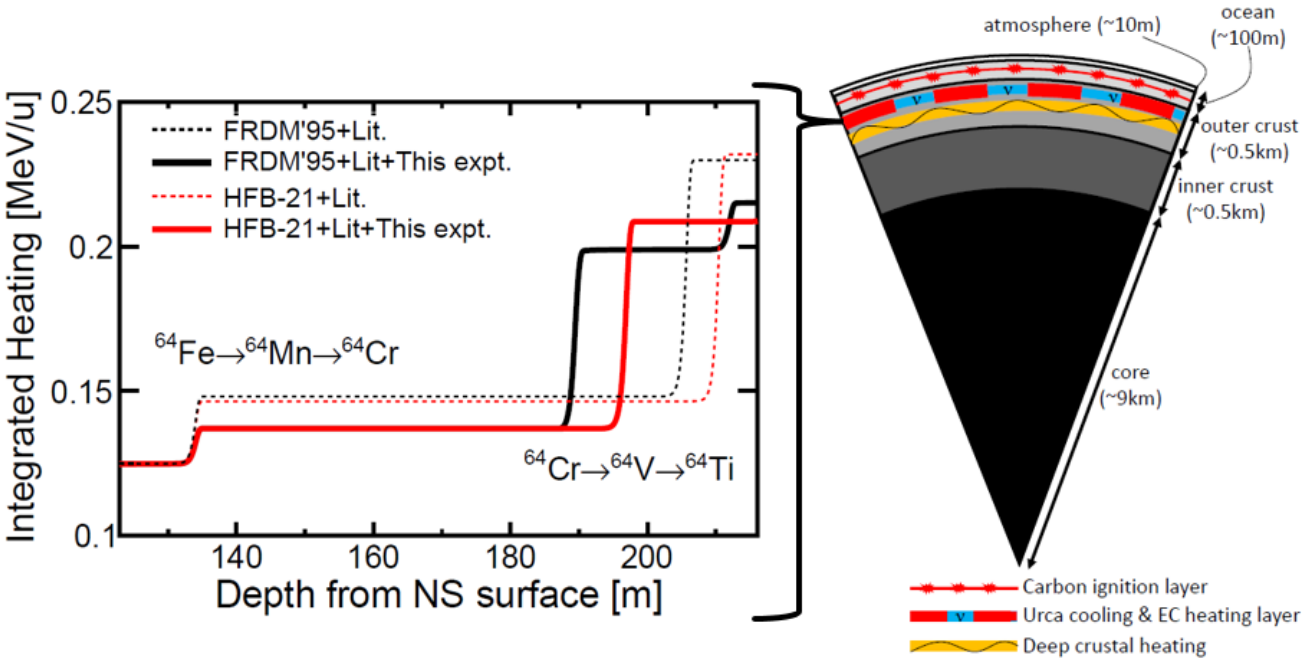

FIG. 15. (color online.) Integrated heat release in MeV per accreted nucleon from electron capture for an $A = 64$ fluid element as a function of depth (left panel) in the region where the ^{64}Fe $\rightarrow^{64}$ Mn $\rightarrow^{64}$ Cr and ^{64}Cr $\rightarrow^{64}$ V $\rightarrow^{64}$ Ti compositional transitions occur, schematically indicated with respect to deep crustal heating [75] and the carbon ignition layer where x-ray superbursts are powered [24] in the right panel, where the neutron star crust nuclear reaction network and quasiparticle random phase approximation (QRPA) Gamow-Teller transition strength distributions reported in Ref. [58] were used. The calculations corresponding to the black and red lines employed the 1995 FRDM [55] and HFB-21 [56] global mass models for nuclides with unknown masses, where the 2012 Atomic Mass Evaluation [29] was used otherwise. Calculations indicated by solid lines included the mass of ^{64}Cr presented here.

ated astronomical observables [17–19, 26, 58, 76]. Recent calculations with a state-of-the-art multi-zone x-ray burst model have shown that $A = 64$ nuclides dominate the crust composition for a wide set of astrophysical conditions (and varied nuclear physics assumptions) that are thought to correspond to typical x-ray bursting systems [77] and previous work has also demonstrated large $A = 64$ production for stable-burning and superbursting systems [14, 16]. In large part due to this prevalence, Ref. [17] identified the ^{64}Cr $\rightarrow^{64}$ V $\rightarrow^{64}$ Ti electron-capture sequence as one of the main sources of heat (along with neutron-capture reactions) at the lower extent of the outer crust (i.e. at electron Fermi energy $E_{\rm F} \geq 18.5$ MeV). Though weaker than deep crustal heating sources [75], the shallower depth of this heat source makes it important to consider when calculating the layer at which carbon ignites to power x-ray superbursts, as shown schematically in the right panel of Fig. 15.

We performed calculations with a crust composition evolution model [17, 58] in order to assess the impact of our newly measured ^{64}Cr mass on heat release in the accreted neutron star outer crust. The model evolves the composition of an accreted fluid element via nuclear reactions with increasing pressure $p = \dot{m}gt$ (and therefore increasing $E_{\rm F}$), where the accretion rate $\dot{m} = 2.64 \times 10^4 {\rm g\,cm^{-2}\,s^{-1}}$ ($\approx 0.3\ \dot{M}_{\rm Eddington}$ for a 10 km radius 1.4 solar mass neutron star), surface gravity $g = 1.85 \times 10^{14} {\rm cm\,s^{-2}}$, and time t, at a constant temperature of $T = 0.5$ GK, mimicking the effect of a fluid element being naturally buried into the crust via subsequently accreted material. The crust temperature corresponds to the equilibrium value calculated by Ref. [17] and the astrophysical conditions are within the range inferred for the present population of observed formerly-accreting cooling neutron stars [78]. The nuclear reaction network includes electron-capture, β-decay, neutron capture and emission, and fusion reactions.

The resultant integrated nuclear energy release profiles as a function of depth into the neutron star from our calculations are shown in Fig. 15 using our ^{64}Cr mass and the ^{64}Cr masses from the commonly used global mass models FRDM'95 [55] and HFB-21 [56]. The more than 1 MeV reduction in binding we observe for ^{64}Cr with respect to FRDM and HFB-21, a $\sim 3\sigma$ deviation using our experimental uncertainty, results in a substantially reduced odd-even mass staggering for both the Fe–Mn–Cr and Cr–V–Ti $A = 64$ sequences, which reduces the heat release from both electron capture sequences [17, 19]. Additionally, the reduced ^{64}Cr binding energy leads to an earlier transition to ^{64}Cr and therefore a shallower depth for the heat deposition from the ^{64}Cr $\rightarrow^{64}$ V $\rightarrow^{64}$ Ti electron-capture sequence. We note however that the

masses of ^{64}V and ^{64}Ti must be experimentally determined to confirm our conclusions for this second electron-capture sequence.

VI. CONCLUSIONS

We performed time-of-flight nuclear mass measurements of the $A = 59 - 64$ isotopes of chromium at the NSCL at Michigan State University, where the mass of ^{64}Cr was determined for the first time. Our results demonstrate a different behavior with respect to the 2012 AME for the S_{2n} trend in the chromium isotopes approaching $N = 40$, indicating the shape transition from spherical to deformed begins at $N = 38$ rather than $N = 36$. This S_{2n} trend difference is primarily due to the discrepancy between our measured and the 2012 AME evaluated masses for $^{59-61}$Cr. Our ^{64}Cr mass extends the S_{2n} trend for the chromium isotopes to $N = 40$ for the first time, revealing a trend in mass systematics which is consistent with the previously inferred collective behavior of chromium in this region. We find a reduction in binding energy for ^{64}Cr of 1.47 MeV and 1.25 MeV with respect to the global mass models FRDM'95 and HFB-21, respectively, which are commonly used in astrophysics simulations. Based on our experimental mass uncertainty, these differences correspond to a $\sim 3\sigma$ deviation. This reduction in binding energy leads to a reduced odd-even mass stagger near chromium in the $A = 64$ isobaric chain, ultimately causing a reduction of the magnitude and depth of electron-capture heating associated with ^{64}Cr, a major heat source in the outer crust of accreting neutron stars. Additionally, we performed state-of-the-art shell-model calculations to calculate S_{2n} for the chromium isotopic chain, demonstrating the importance of including the $g_{9/2}$ and $d_{5/2}$ neutron valence spaces for shell-model calculations in this region. Future high-precision (e.g. Penning trap) mass measurements of scandium and vanadium isotopes in this region will enable a reevaluation of the presented data, likely reducing the systematic uncertainty of our chromium masses. In order to conclusively determine the magnitude of electron-capture heating in the $A = 64$ isobaric chain, the masses of ^{64}V and ^{64}Ti will need to be measured.

ACKNOWLEDGMENTS

We thank C. Morse, C. Prokop, and J. Vredevoogd for many useful discussions. This project is funded by the NSF through Grants No. PHY-0822648, PHY-1102511, PHY-1404442, and No. PHY-1430152. S.G. acknowledges support from the DFG under Contracts No. GE2183/1-1 and No. GE2183/2-1.

[1] B. A. Brown, Prog. Part. Nucl. Phys. **47**, 517 (2001).
[2] R. V. F. Janssens, Phys. Scr. **T152**, 014005 (2013).
[3] J. Erler *et al.*, Nature (London) **486**, 509 (2012).
[4] O. Sorlin *et al.*, Euro. Phys. Jour. A **16**, 55 (2003).
[5] A. Gade *et al.*, Phys. Rev. C **81**, 051304(R) (2010).
[6] T. Baugher *et al.*, Phys. Rev. C **86**, 011305(R) (2012).
[7] S. Naimi *et al.*, Phys. Rev. C **86**, 014325 (2012).
[8] H. L. Crawford *et al.*, Phys. Rev. Lett. **110**, 242701 (2013).
[9] T. Braunroth *et al.*, Phys. Rev. C **92**, 034306 (2015).
[10] P. Adrich, A. M. Amthor, D. Bazin, M. D. Bowen, B. A. Brown, C. M. Campbell, J. M. Cook, A. Gade, D. Galaviz, T. Glasmacher, S. McDaniel, D. Miller, A. Obertelli, Y. Shimbara, K. P. Siwek, J. A. Tostevin, and D. Weisshaar, Phys. Rev. C **77**, 054306 (2008).
[11] S. M. Lenzi, F. Nowacki, A. Poves, and K. Sieja, Phys. Rev. C **82**, 054301 (2010).
[12] D. Lunney, J. M. Pearson, and C. Thibault, Rev. Mod. Phys. **75**, 1021 (2003).
[13] Z. Meisel *et al.*, Phys. Rev. Lett. **114**, 022501 (2015).
[14] H. Schatz, L. Bildsten, A. Cumming, and M. Wiescher, Astrophys. J. **524**, 1014 (1999).
[15] H. Schatz *et al.*, Phys. Rev. Lett. **86**, 3471 (2001).
[16] H. Schatz, L. Bildsten, and A. Cumming, Astrophys. J. Lett. **583**, L87 (2003).
[17] S. Gupta, E. F. Brown, H. Schatz, P. Möller, and K.-L. Kratz, Astrophys. J. **662**, 1188 (2007).
[18] A. Estradé *et al.*, Phys. Rev. Lett. **107**, 172503 (2011).
[19] Z. Meisel *et al.*, Phys. Rev. Lett. **115**, 162501 (2015).
[20] S. E. Woosley and R. E. Taam, Nature (London) **263**, 101 (1976).
[21] H. Schatz and K. Rehm, Nucl. Phys. A **777**, 601 (2006).
[22] A. Parikh, J. José, G. Sala, and C. Iliadis, Prog. Part. Nucl. Phys. **69**, 225 (2013).
[23] A. Cumming and L. Bildsten, Astrophys. J. Lett. **559**, L127 (2001).
[24] L. Keek, A. Heger, and J. J. M. in 't Zand, Astrophys. J. **752**, 150 (2012).
[25] E. F. Brown and A. Cumming, Astrophys. J. **698**, 1020 (2009).
[26] A. Deibel, A. Cumming, E. F. Brown, and D. Page, Astrophys. J. Lett. **809**, L31 (2015).
[27] L. Bildsten, Astrophys. J. Lett. **501**, L89 (1998).
[28] G. Ushomirsky, C. Cutler, and L. Bildsten, Mon. Not. R. Astron. Soc. **319**, 902 (2000).
[29] G. Audi, M. Wang, A. Wapstra, F. Kondev, M. MacCormick, X. Xu, and B. Pfeiffer, Chin. Phys. C **36**, 1287 (2012).
[30] Z. Meisel and S. George, Int. J. Mass Spectrom. **349-350**, 145 (2013).
[31] L. Gaudefroy *et al.*, Phys. Rev. Lett. **109**, 202503 (2012).
[32] M. Matoš *et al.*, Nucl. Instrum. Methods Phys. Res., Sect. A **696**, 171 (2012).
[33] D. J. Morrissey, B. M. Sherrill, M. Steiner, A. Stolz, and I. Wiedenhoever, Nucl. Instrum. Methods Phys. Res., Sect. B **204**, 90 (2003).
[34] D. Bazin, J. Caggiano, B. Sherrill, J. Yurkon, and A. Zeller, Nucl. Instrum. Methods Phys. Res., Sect. B

204, 629 (2003).
[35] J. Yurkon *et al.*, Nucl. Instrum. Methods Phys. Res., Sect. A **422**, 291 (1999).
[36] R. York *et al.*, in *Cyclotrons and Their Applications 1998*, edited by E. Baron and M. Liuvin (Institute of Physics Publishing, 1999) pp. 687–691, Proceedings of the 15th International Conference, Caen, France, 14-19 June 1998.
[37] "http://www.crystals.saint-gobain.com," Saint-Gobain Crystals.
[38] "http://www.hamamatsu.com," Hamamatsu Photonics.
[39] "http://www.belden.com," Belden CDT Inc.
[40] Z. Meisel, *Extension of the nuclear mass surface for neutron-rich isotopes of argon through iron*, Ph.D. thesis, Michigan State University, East Lansing (2015).
[41] D. Shapira, T. Lewis, and L. Hulett, Nucl. Instrum. Methods Phys. Res., Sect. A **454**, 409 (2000).
[42] "http://www.quantar.com," Quantar Technology Inc.
[43] "http://www.magnetsales.com," Magnet Sales and Manufacturing Inc.
[44] M. Jung, H. Rothard, B. Gervais, J.-P. Grandin, A. Clouvas, and R. Wünsch, Phys. Rev. A **54**, 4153 (1996).
[45] L. Landau and E. Lifshitz, *The Classical Theory of Fields*, 4th ed. (Elsevier, 1975) Part of the *Course of Theoretical Physics, Volume 2*.
[46] A. M. Rogers *et al.*, Nucl. Instrum. Methods Phys. Res., Sect. A **795**, 325 (2015).
[47] "https://root.cern.ch/drupal/," ROOT Data Analysis Framework.
[48] F. Wienholtz *et al.*, Nature (London) **498**, 346 (2013).
[49] "http://www.nndc.bnl.gov/," National Nuclear Data Center compilation, Accessed January 2014.
[50] W. Lotz, Journal of the Optical Society of America **60**, 206 (1970).
[51] L. Chen *et al.*, Nuc. Phys. A **882**, 71 (2012).
[52] X. Tu *et al.*, Z. Phys. A **337**, 361 (1990).
[53] H. Seifert *et al.*, Z. Phys. A **349**, 25 (1994).
[54] Y. Bai, D. J. Vieira, H. L. Seifert, and J. M. Wouters, AIP Conf. Proc. **455** (1998).
[55] P. Möller, J. Nix, W. Myers, and W. Swiatecki, At. Data Nucl. Data Tables **59**, 185 (1995).
[56] S. Goriely, N. Chamel, and J. M. Pearson, Phys. Rev. C **82**, 035804 (2010).
[57] J. M. Pearson, S. Goriely, and N. Chamel, Phys. Rev. C **83**, 065810 (2011).
[58] H. Schatz *et al.*, Nature (London) **505**, 62 (2014).
[59] M. Honma, T. Otsuka, B. A. Brown, and T. Mizusaki, Euro. Phys. Jour. A **25**, 499 (2005).
[60] S. Raman, C.W. Nestor Jr., and P. Tikkanen, At. Data Nucl. Data Tables **78**, 1 (2001).
[61] N. Mărginean *et al.*, Phys. Lett. B **633**, 696 (2006).
[62] V. Werner *et al.*, Euro. Phys. Jour. Web Conf. **107**, 03007 (2016), Proceedings of the International Conference on Nuclear Structure and Related Topics 2015, Dubna, Russia.
[63] M. Rosenbusch *et al.*, Phys. Rev. Lett. **114**, 202501 (2015).
[64] F. Iachello, A. Leviatan, and D. Petrellis, Phys. Lett. B **705**, 379 (2011).
[65] A. Chaudhuri *et al.*, Phys. Rev. C **88**, 054317 (2013).
[66] B. V. Pritychenko *et al.*, Phys. Lett. B **461**, 322 (1999).
[67] J. R. Terry *et al.*, Phys. Rev. C **77**, 014316 (2008).
[68] K. Wimmer *et al.*, Phys. Rev. Lett. **105**, 252501 (2010).
[69] A. Deacon *et al.*, Phys. Lett. B **622**, 151 (2005).
[70] S. Zhu *et al.*, Phys. Rev. C **74**, 064315 (2006).
[71] T. Togashi, N. Shimizu, Y. Utsuno, T. Otsuka, and M. Honma, Phys. Rev. C **91**, 024320 (2015).
[72] E. Sahin *et al.*, Phys. Rev. C **91**, 034302 (2015).
[73] P. Morfouace *et al.*, Phys. Lett. B **751**, 306 (2015).
[74] S. Suchyta *et al.*, Phys. Rev. C. **89**, 034317 (2014).
[75] A. W. Steiner, Phys. Rev. C **85**, 055804 (2012).
[76] A. Deibel, Z. Meisel, H. Schatz, E. F. Brown, and A. Cumming, "Urca cooling pairs in the neutron star ocean and their effect on superburst cooling," (2016), *Submitted*.
[77] R. H. Cyburt, A. M. Amthor, A. Heger, E. Johnson, Z. Meisel, H. Schatz, and K. Smith, "Dependence of x-ray burst models on nuclear reaction rates," (2015), *Submitted*.
[78] A. Turlione, D. N. Aguilera, and J. A. Pons, Astron. & Astrophys. **577**, A5 (2015).